

# Electronically-driven switching of topology in LaSbTe

J. Bannies,<sup>1,2,\*</sup> M. Michiardi,<sup>1,3</sup> H.-H. Kung,<sup>1,3</sup> S. Godin,<sup>1,3</sup> J. W. Simonson,<sup>4</sup> M. Oudah,<sup>1</sup> M. Zonno,<sup>5</sup> S. Gorovikov,<sup>5</sup> S. Zhdanovich,<sup>1,3</sup> I. S. Elfimov,<sup>1,3</sup> A. Damascelli,<sup>1,3,†</sup> and M. C. Aronson<sup>1,3,‡</sup>

<sup>1</sup>*Quantum Matter Institute, University of British Columbia,  
Vancouver, British Columbia, V6T 1Z4, Canada*

<sup>2</sup>*Department of Chemistry, University of British Columbia,  
Vancouver, Canada V6T 1Z1, Canada*

<sup>3</sup>*Department of Physics & Astronomy,  
University of British Columbia, Vancouver,  
British Columbia, V6T 1Z1, Canada*

<sup>4</sup>*Department of Physics, Farmingdale State College, Farmingdale, NY 11735, USA*

<sup>5</sup>*Canadian Light Source Inc., Saskatoon, Saskatchewan, S7N 2V3, Canada*

(Dated: July 15, 2024)

## Abstract

In the past two decades, various classes of topological materials have been discovered, spanning topological insulators, semimetals, and metals. While the observation and understanding of the topology of a material has been a primary focus so far, the precise and easy control of topology in a single material remains largely unexplored. Here, we demonstrate full experimental control over the topological Dirac nodal loop in the square-net material  $\text{LaSb}_x\text{Te}_{2-x}$  by chemical substitution and electron doping. Using angle-resolved photoemission spectroscopy (ARPES), we show that changing the antimony concentration  $x$  from 0.9 to 1.0 in the bulk opens a gap as large as 400 meV in the nodal loop. Our symmetry analysis based on single-crystal X-ray diffraction and a minimal tight binding model establishes that the breaking of  $n$  glide symmetry in the square-net layer is responsible for the opening of the gap. Remarkably, we can also realize this topological phase transition *in situ* on the surface of  $\text{LaSb}_x\text{Te}_{2-x}$  by chemical gating using potassium deposition, which enables the reversible switching of the topology from gapped to gapless nodal loop. The underlying control parameter for the structural and topological transition in the bulk and on the surface is the electron concentration. It opens a pathway towards applications in devices based on switching topology by electrostatic gating.

## INTRODUCTION

Symmetry is key to understanding the low-energy electronic structure of topological materials, which are generally characterized by a non-zero topological invariant. The existence of Dirac fermions in condensed matter systems, for example, is protected by time-reversal symmetry [1, 2] or crystalline symmetry [3]. Many of the exotic phenomena found in topological materials are related to the Dirac fermions near the Fermi level, such as the quantum spin Hall effect in two-dimensional topological insulators [4–6], quantum anomalous Hall effect in magnetically-doped topological insulators [7], or extremely large magnetoresistance in Dirac semimetals [8]. To harness these effects for device applications, it is crucial to control the topology of a material, rather than simply observing it.

In the most fundamental case, one can imagine driving a topological phase transition

from the topologically trivial state to the non-trivial state by external input. To achieve such a topological phase transition, it is desirable to find a way to tune the symmetry that protects the topological phase. Successful attempts to destabilize the topological phase include the gap opening at the surface Dirac cone in topological insulators by breaking of time-reversal symmetry [7, 9, 10], and in topological crystalline insulators by breaking mirror symmetry on the surface [11]. Similarly, topological phase transitions were achieved in topological insulators by continuously tuning the strength of spin-orbit coupling via bulk chemical substitution [12–14]. However, all these realizations of topological phase transitions rely on bulk chemical substitution, which is an irreversible process that cannot be triggered and controlled by external input.

To fully exploit the considerable promises of future technologies based on topological materials, it is important to find a fast and reliable switching knob that can turn the topological states on and off. To be in accord with current state-of-the-art, an electronically-driven process is the most desirable since it can be controlled by fast switching of electric fields. Such a process was demonstrated in quantum-confined  $\text{Na}_3\text{Bi}$  [15]; however, the extreme air sensitivity of  $\text{Na}_3\text{Bi}$  is unfavorable for applications.

Here, we report the electronically-driven opening of a large gap in the Dirac nodal loop of the square-net material  $\text{LaSb}_x\text{Te}_{2-x}$ . Increasing  $x$  from 0.9 to 1 by bulk chemical substitution leads to a structural phase transition that breaks the  $n$  glide symmetry of the square-net layer by distortion into zig-zag chains. Combining angle-resolved photoemission spectroscopy (ARPES) with tight binding simulations, we establish that this symmetry breaking triggers a topological phase transition from gapless to gapped nodal loop. Importantly, we can also realize the opening and closing of the gap *in situ* by chemical gating of the surface of  $\text{LaSb}_x\text{Te}_{2-x}$ . The electronic nature of the transition opens the possibility of straightforward control of the nodal loop topology by electrostatic gating in devices based on  $\text{LaSb}_x\text{Te}_{2-x}$  thin films.

## MAIN

To understand which symmetries need to be broken to lift the topological protection of the nodal loop, we consider a simple model consisting of a square-net with a body-centered two-dimensional square lattice as shown in Fig. 1a. It can be described by two equivalent

sublattices A and B, which are related by non-symmorphic  $n$  glide symmetry - a mirror operation  $M_z$  followed by a  $(1/2, 1/2)$  lattice translation. We build a minimal tight binding model of this square lattice that uses only the  $p_{x,y}$  orbitals. Distances and electron fillings were chosen to most closely represent the system under study in this work. It is known that the body-centering of the unit cell imposes a band folding that gives rise to degenerate band crossings [16] as visible in Fig. 1b. We study the effect of symmetry lowering in this ideal square-net (Fig. 1a) in two steps, by first removing fourfold symmetry and then  $n$  glide symmetry, and track the changes in the band structure as well as the Fermi surface (Figs. 1b,c).

The band structure of the undistorted square-net is dominated by linear band crossings close to the Fermi level. These crossings are part of a nodal loop that spans the entire diamond-shaped Fermi surface and is protected by  $n$  glide symmetry. The breaking of fourfold symmetry only has minor effects on the band structure, and importantly the nodal loop remains gapless because  $n$  glide symmetry still translates atom A into atom B. However, subsequent displacement of atom B from the center of the unit cell breaks  $n$  glide symmetry, forming zig-zag chains and making the sublattices inequivalent. This symmetry lowering lifts the degeneracy and creates a gap in the nodal loop. The size of the gap depends on the degree of displacement of atom B; for the experimental value of the system under study, we obtain a large gap of several hundred meV. Correspondingly, the diamond-shaped Fermi surface disappears and only small electron pockets survive at the Brillouin zone boundary. Importantly, these pockets are formed from parabolic bands, in contrast to the linear bands of the original square-net. Our minimal model highlights the requirement of breaking  $n$  glide symmetry as the mechanism to gap the nodal loop, and also shows the resulting drastic change in the Fermi surface. It furthermore suggests that a change in crystalline symmetry between these extreme cases of square-net and zig zag chains causes the massless Dirac fermions to acquire a finite mass term. Breaking the  $n$  glide symmetry experimentally, however, is not a trivial feat in square-net materials as it requires breaking fourfold symmetry, and at the same time selectively displacing the center atom of the unit cell.

To this end, we consider the curious case of the  $\text{RE}\text{Sb}_x\text{Te}_{2-x}$  (RE=rare-earth) systems, which feature a square-net of antimony atoms and are known for their rich phase diagrams [17–20], including a tetragonal to orthorhombic transition as a function of chemical

substitution of antimony by tellurium [18–21]. We choose the specific case of  $\text{LaSb}_x\text{Te}_{2-x}$  as the simplest system that is non-magnetic and is not subject to electronic correlation effects. We grew single crystals of  $\text{LaSb}_x\text{Te}_{2-x}$  and determined their structure and composition by single crystal X-ray diffraction (XRD) and wavelength dispersive X-ray spectroscopy. Remarkably, we find that the square-net layer in  $\text{LaSb}_x\text{Te}_{2-x}$  undergoes both symmetry lowering transitions required to realize our minimal square-net model, by simply changing the antimony concentration  $x$ , which is equivalent to changing the electron filling of the square-net. Our single crystal XRD data evince the selective breaking of fourfold and  $n$  glide symmetry in a narrow window of  $0.7 < x < 1$ , as shown in Fig. 1d, resulting in two distinct orthorhombic phases in close vicinity to an intermediate tetragonal phase.

Here, we focus on two neighboring phases of  $\text{LaSb}_x\text{Te}_{2-x}$ : tetragonal  $\text{LaSb}_{0.86}\text{Te}_{1.14}$  with a gapless nodal loop, and orthorhombic  $\text{LaSbTe}$  with a gapped nodal loop. Single-crystal structure refinements (see SM) show that the former is characterized by an ideal antimony square-net layer with  $n$  glide symmetry, whereas the latter features antimony zig-zag chains, i.e. broken  $n$  glide symmetry, in the antimony layer (Fig. 1e,f). From here on, we refer to these materials as  $t$ - $\text{LaSbTe}$  and  $o$ - $\text{LaSbTe}$ . We probe the band structure of the two phases of  $\text{LaSb}_x\text{Te}_{2-x}$  by employing ARPES on single crystals of both  $o$ - $\text{LaSbTe}$  and  $t$ - $\text{LaSbTe}$ .

In Fig. 2a,b we present an overview of the band structures of  $t$ - $\text{LaSbTe}$  and  $o$ - $\text{LaSbTe}$  measured over a wide energy window. For  $t$ - $\text{LaSbTe}$ , linear bands cross the Fermi level along  $\Gamma$ -X and  $\Gamma$ -M. As expected from our minimal model, those bands are gapped by several hundred meV at X and along  $\Gamma$ -M in  $o$ - $\text{LaSbTe}$  due to the broken  $n$  glide symmetry. These differences are also reflected in the Fermi surfaces of the two phases, see Fig. 2c,d. In  $t$ - $\text{LaSbTe}$ , the linear bands form two concentric diamond-shaped Fermi surface sheets, whereas the Fermi surface of  $o$ - $\text{LaSbTe}$  only consists of two small electron pockets. These observations demonstrate the experimental realization of our square-net model, and their excellent agreement with complementary band structure calculations based on density functional theory (DFT).

Furthermore, we observe a strong dependence of the intensity of the nodal loop bands on the polarization of the incident light for  $t$ - $\text{LaSbTe}$ : linear horizontal (LH) and linear vertical (LV) polarizations couple to opposite branches of the nodal loop, see Fig. 2e. The observed bands are gapless and linear with high Fermi velocities of  $8.8(1) \text{ eV}\cdot\text{\AA}^{-1}$ , in agreement with previous reports [22]. In contrast, the nodal loop is gapped by at least 400 meV along  $\Gamma$ -M in

*o*-LaSbTe, regardless of the light polarization, as seen in Fig. 2f. We define this lower bound by the valence band maximum energy with respect to the Fermi level, as we cannot probe the unoccupied conduction band states and therefore the conductivity gap directly in ARPES experiments. In addition, we observe a splitting of the valence band, which we attribute to the presence of two antimony layers per unit cell in *o*-LaSbTe (Fig. 1f). A similar bilayer splitting was found in related square-net materials such as rare-earth tritellurides [23, 24].

The opening of a gap by changing the crystalline symmetry of  $\text{LaSb}_x\text{Te}_{2-x}$  via small variation in composition is the direct experimental demonstration that *n* glide symmetry indeed protects the existence of the nodal loop in ideal square-net materials.

The doping dependence of the phase transition presents itself as a unique opportunity to study the origin of this transition. Because small changes in composition induce a phase transition, we can try to understand whether it is caused by the chemical pressure effect induced by chemical substitution of antimony by tellurium, or rather by the effective electron doping accompanying the substitution. If the transition is electronically-driven, it will allow for much easier and faster switching between the phases, such as by gating the material. Here, we demonstrate that the small tellurium excess needed to stabilize *t*-LaSbTe is equivalent to electron-doping the square-net layer. We emulate this property of the bulk material using *in situ* chemical gating by stepwise potassium deposition to electron-dope the surface of *o*-LaSbTe. We track the evolution of the electronic structure across the transition by measuring the Fermi surface and the  $\Gamma$ -M cut at each deposition step, as shown in Fig. 3a, b.

In the initial stages of the potassium deposition, the valence bands shift down in energy and the Fermi surface volume increases, indicating a rigid band shift of the Fermi level caused by the electron doping. However, starting from step 3, a qualitatively different behavior sets in. The Fermi surface undergoes a gradual redistribution of spectral weight and representative energy distribution curves (Fig. 3c) show the appearance of in-gap states in the nodal loop gap. Increasing the doping leads the nodal loop gap to collapse completely and the Fermi surface becomes fourfold symmetric, in stark contrast to the twofold symmetric Fermi surface of pristine *o*-LaSbTe. In addition, the bilayer splitting, characteristic of broken *n* glide symmetry, disappears as the in-gap states fill the entire gap (see Fig. 3d). Effectively, the band structure of chemically gated *o*-LaSbTe resembles that of bulk *t*-LaSbTe, indicating a surface structural transition into the topological nodal loop phase that is driven by an

increase of electrons at the surface. This doping-controlled structural transition of the *o*-LaSbTe surface is therefore the analog of the bulk structural phase transition between *o*-LaSbTe and *t*-LaSbTe, for which electron doping is achieved by decreasing the antimony concentration  $x$ .

Remarkably, the *in situ* doping-driven phase transition is shown to be completely reversible by desorbing the potassium from the sample surface (see Methods). As shown in Fig. 3e, the system transitions continuously back into the pristine surface of *o*-LaSbTe, breaking the  $n$  glide symmetry and restoring the gap in the nodal loop.

The surface phase transition is characterized by a complex band structure change in the intermediate phase that encodes the microscopic mechanism underlying such behavior. To understand this change better, we probe the polarization dependence by using LH and LV polarizations similar to bulk *t*-LaSbTe and *o*-LaSbTe. The resulting band dispersions are presented in Fig. 4a. In dosing steps 4 and 5, the in-gap states exhibit Dirac-like dispersion even though the nodal loop still exhibits a gap. These Dirac in-gap states move down in energy upon increasing electron doping; concomitantly, the bandwidth of the in-gap states increases until they span the entire gap in the fully dosed state in step 6. Our model (Fig. 1a) provides no mechanism for in-gap states within the nodal loop gap. We conclude that the phase transition is accompanied by a more complex behavior than the simple simultaneous displacement of the central antimony atoms. The experimental observation of band folding in the in-gap states suggests an additional transition involving a charge density wave (CDW) phase. Indeed, CDW instabilities are commonly found in square-net materials. [17, 19, 23–26].

For a qualitative description of the observed behavior, we construct model CDWs using only antimony atoms in a supercell approach and calculate their electronic structure in the framework of DFT. Starting from the unit cell of a perfect square-net, we introduce a sinusoidal modulation of the center antimony’s  $y$  coordinate in each subcell, as illustrated for a 7x1x1 structure in Fig. 4b. For simplicity, we focus on the unfolded band structure along  $\Gamma$ -M for several supercells of different size. For the 11x1x1 supercell, the Dirac cone characteristic for *t*-LaSbTe is broken up by several gaps such that the bandwidth of the subbands around the Dirac cone is reduced compared to the unperturbed Dirac cone (see Fig. 4c). The band folding at the edges of the subbands is a hallmark of the CDW and resembles the band folding of the in-gap states in our experimental data. Moreover, the bandwidth

of the calculated in-gap states increases as the size of the supercell decreases until the gapless ideal square-net in the 1x1x1 cell is reached, reproducing the experimentally observed trend. We estimate that the intermediate CDW phases of the potassium-doped surface have supercell sizes on the order of 10-20 unit cells. Because the center subcell for each model supercell is a perfect square ( $y = 0.5$ ) that is equivalent to that of  $t$ -LaSbTe, the size of the supercell effectively controls the fraction of unit cells that remains distorted. The increasing bandwidth of the in-gap states with doping thus indicates the gradual restoration of  $n$  glide symmetry in the surface antimony layer, allowing for a continuous tuning of symmetry that does not seem to have a counterpart in the bulk materials, where  $n$  glide symmetry in the antimony layer either exists or not. A similar doping dependence of CDW supercell size was observed previously in  $\text{RESb}_x\text{Te}_{2-x}$  systems [17–19] but only in bulk samples, and the resulting changes to the band structure were not explored.

Our study provides convincing evidence that electron doping causes a phase transition both in bulk (via chemical substitution) and on the surface (via chemical gating) of  $\text{LaSb}_x\text{Te}_{2-x}$  through restoration of  $n$  glide symmetry in the antimony layer. While the transition is robust against the disorder that necessarily accompanies bulk chemical substitution, the electron doping at the surface is a cleaner, reversible, and versatile way to control the topological states. This supports the conclusion that the phase transition from  $o$ -LaSbTe to  $t$ -LaSbTe is electronically driven, and more generally that the electron concentration is the primary control parameter for the structural and topological transitions in  $\text{LaSb}_x\text{Te}_{2-x}$ .

## CONCLUSION

In summary, we have demonstrated an efficient way to manipulate the nodal loop topology in square-net materials. Exploiting the structural instabilities in  $\text{LaSb}_x\text{Te}_{2-x}$ , we break the  $n$  glide symmetry that protects the nodal loop by changing the antimony concentration  $x$ . As evidenced in bulk materials with  $x=0.9$  and  $x=1$ , the breaking of  $n$  glide symmetry opens a gap of several hundred meV in the nodal loop, manifesting a drastic change of the topology from gapless to heavily gapped nodal loop. The control parameter for this transition is the electron concentration of the square-net layer, which opens the possibility of control by gating. Here, we used chemical gating of the surface by potassium deposition to realize the reversible switching between the two topologically distinct phases. The full reversibility of

the gap closing is a pre-condition for effective switching of topology between gapless and gapped nodal loop in devices. Taking our chemical gating study as a proof of concept, we expect that electrostatic gating can be used to control the topological phase transition in  $\text{LaSb}_x\text{Te}_{2-x}$  thin films, allowing for wider doping regimes and more facile device integration. Our findings point to a promising avenue towards devices that exploit transitions between topologically distinct states, a crucial step forward to a new family of devices based on the exotic properties of topological materials.

## METHODS

**Single crystal growth.** Single crystals of *o*-LaSbTe were grown using the liquid transport method, inspired by Ref. [27]. Elements were weighed in a 1:15:2-x ratio (La:Sb:Te) and sealed in a quartz glass tube under 0.3 bar argon. The mixture was then heated to 910 °C and kept in a horizontal gradient from 910 °C to 770 °C for 10-14 days before cooling to room temperature at a rate of 50 K/h. Crystals were separated from the solidified flux after heating the mixture to 700 °C for 20 min and then spinning. *t*-LaSbTe was grown by chemical vapor transport. Elements were weighed in a 1:5:1 ratio (La:Sb:Te) with an addition of 100 mg iodine and sealed in a quartz glass tube under vacuum. The mixture was pre-reacted at 800 °C for one week and then subjected to a temperature gradient from 910 °C to 800 °C for two weeks with the crystals forming in the hot end.

**Characterization.** The phase purity of the crystals was checked with powder XRD. Patterns on ground single crystals were acquired with a Bruker D8 using  $\text{Cu K}\alpha_1$  radiation. The crystal structures of *o*-LaSbTe and *t*-LaSbTe were solved from single crystal XRD. Data were acquired with a Rigaku XtaLAB mini II using  $\text{Mo K}\alpha$  radiation and the structures were refined by a standard charge-flipping method. The composition of the crystals was determined by wavelength dispersive X-ray spectroscopy.

**ARPES measurements.** Measurements were conducted at the Quantum Materials Spectroscopy Center (QMSC) beamline at the Canadian Light Source. Samples were cleaved and measured at  $T=20$  K and a base pressure of  $6 \cdot 10^{-11}$  torr using 87 eV photons, unless mentioned otherwise. The angular resolution was 0.1 ° and the energy resolution was about 30 meV. *In situ* potassium deposition was performed in six steps for 5 s, 5 s, 5 s, 15 s, 30 s, and 60 s (steps 1-6 in Fig. 3a) at  $T=20$  K using a getter source from SAES.

For potassium desorption experiments, the sample was transferred into an oven inside the ultra-high vacuum chamber and heated in three steps (15 min at 100 °C, 15 min at 120 °C, and 45 min at 130 °C). The pressure during this procedure did not exceed  $4 \cdot 10^{-10}$  torr. After each heating step, the sample was transferred back into the cryostat and cooled to 20 K, followed by acquisition of the spectra.

**DFT calculations.** Electronic structure calculations were performed within the framework of DFT as implemented in the package WIEN2k [28, 29]. The generalized gradient approximation with the Perdew-Burke-Ernzerhof parametrization [30] was used. The basis set size was set to  $R_{\text{mt}}K_{\text{max}}=8.5$  and the Brillouin zone was sampled with 6000 k points. The results of these calculations were cross-checked with Quantum Espresso [31, 32]. Furthermore, supercell calculations presented in Fig. 4c were performed using Quantum Espresso. The plane wave expansion was cut off at 60 Ryd and the Brillouin zone was sampled with about 1 k point per  $0.1 \text{ \AA}^{-1}$ .

## ACKNOWLEDGEMENTS

We thank Anette von der Handt (UBC Earth Sciences) for assistance with the wavelength dispersive X-ray spectroscopy measurements. This research was undertaken thanks in part to funding from the Max Planck-UBC-UTokyo Centre for Quantum Materials and the Canada First Research Excellence Fund, Quantum Materials and Future Technologies Program. This project is also funded by the Natural Sciences and Engineering Research Council of Canada (NSERC); Canada Foundation for Innovation (CFI); the British Columbia Knowledge Development Fund (BCKDF); the Department of National Defence (DND); the Mitacs Accelerate Program; the Moore EPiQS Program (A.D.); the Canada Research Chairs Program (A.D.); and the CIFAR Quantum Materials Program (A.D.). This research is funded in part by a QuantEmX grant from ICAM and the Gordon and Betty Moore Foundation through Grant GBMF9616 to M.M. and H.-H.K. J.B. and H.-H.K. acknowledge the receipt of support from the CLSI Student Travel Support Program. J.W.S. was supported in part by a Provost’s Research Fellowship from Farmingdale State College. Use of the Canadian Light Source (Quantum Materials Spectroscopy Centre), a national research facility of the University of Saskatchewan, is supported by CFI, the NSERC, the National Research Council, the Canadian Institutes of Health Research, the Government of Saskatchewan, and the

University of Saskatchewan.

## AUTHOR CONTRIBUTIONS

JB grew single crystals and characterized them. JWS performed single-crystal XRD and solved the crystal structures. JB, MM, and HHK conducted the ARPES experiments with help from MZ, SGor., and SZ. JB analyzed the ARPES data with input from MM, HHK, and AD. SGod. analyzed the core level spectra. JB performed DFT calculations with help from ISE. JB, MM, HHK, MO, AD, and MCA discussed the results. JB, MM, HHK, AD, and MCA wrote the paper, with contributions from all authors.

## COMPETING INTERESTS

The authors declare they have no competing interests.

## DATA AVAILABILITY

All data needed to evaluate the conclusions in the paper are present in the paper. The raw ARPES data acquired in this study have been deposited in the Zenodo database under the digital object identifier [URL will be inserted for final submission].

---

\* [jbannies@chem.ubc.ca](mailto:jbannies@chem.ubc.ca)

† [damascelli@physics.ubc.ca](mailto:damascelli@physics.ubc.ca)

‡ [meigan.aronson@ubc.ca](mailto:meigan.aronson@ubc.ca)

- [1] H. Zhang, C. X. Liu, X. L. Qi, X. Dai, Z. Fang, and S. C. Zhang, Topological insulators in  $\text{Bi}_2\text{Se}_3$ ,  $\text{Bi}_2\text{Te}_3$  and  $\text{Sb}_2\text{Te}_3$  with a single Dirac cone on the surface, *Nat. Phys.* **5**, 438 (2009).
- [2] M. Z. Hasan and C. L. Kane, Colloquium: Topological insulators, *Rev. Mod. Phys.* **82**, 3045 (2010).
- [3] Y. Ando and L. Fu, Topological crystalline insulators and topological superconductors: From concepts to materials, *Annu. Rev. Condens. Matter Phys.* **6**, 361 (2015).

- [4] B. A. Bernevig, T. L. Hughes, and S. C. Zhang, Quantum spin hall effect and topological phase transition in HgTe quantum wells, *Science* **314**, 1757 (2006).
- [5] M. König, S. Wiedmann, C. Brüne, A. Roth, H. Buhmann, L. W. Molenkamp, X. L. Qi, and S. C. Zhang, Quantum spin hall insulator state in HgTe quantum wells, *Science* **318**, 766 (2007).
- [6] S. Wu, V. Fatemi, Q. D. Gibson, K. Watanabe, T. Taniguchi, R. J. Cava, and P. Jarillo-Herrero, Observation of the quantum spin Hall effect up to 100 kelvin in a monolayer crystal, *Science* **359**, 76 (2018).
- [7] C. Z. Chang, J. Zhang, X. Feng, J. Shen, Z. Zhang, M. Guo, K. Li, Y. Ou, P. Wei, L. L. Wang, Z. Q. Ji, Y. Feng, S. Ji, X. Chen, J. Jia, X. Dai, Z. Fang, S. C. Zhang, K. He, Y. Wang, L. Lu, X. C. Ma, and Q. K. Xue, Experimental observation of the quantum anomalous Hall effect in a magnetic topological Insulator, *Science* **340**, 167 (2013).
- [8] T. Liang, Q. Gibson, M. N. Ali, M. Liu, R. J. Cava, and N. P. Ong, Ultrahigh mobility and giant magnetoresistance in the Dirac semimetal  $\text{Cd}_3\text{As}_2$ , *Nat. Mater.* **14**, 280 (2014).
- [9] Y. L. Chen, J. H. Chu, J. G. Analytis, Z. K. Liu, K. Igarashi, H. H. Kuo, X. L. Qi, S. K. Mo, R. G. Moore, D. H. Lu, M. Hashimoto, T. Sasagawa, S. C. Zhang, I. R. Fisher, Z. Hussain, and Z. X. Shen, Massive dirac fermion on the surface of a magnetically doped topological insulator, *Science* **329**, 659 (2010).
- [10] J. Zhang, C. Z. Chang, P. Tang, Z. Zhang, X. Feng, K. Li, L. L. Wang, X. Chen, C. Liu, W. Duan, K. He, Q. K. Xue, X. Ma, and Y. Wang, Topology-driven magnetic quantum phase transition in topological insulators, *Science* **340**, 1582 (2013).
- [11] I. Zeljkovic, Y. Okada, M. Serbyn, R. Sankar, D. Walkup, W. Zhou, J. Liu, G. Chang, Y. J. Wang, M. Z. Hasan, F. Chou, H. Lin, A. Bansil, L. Fu, and V. Madhavan, Dirac mass generation from crystal symmetry breaking on the surfaces of topological crystalline insulators, *Nat. Mater.* **14**, 318 (2015).
- [12] S. Y. Xu, Y. Xia, L. A. Wray, S. Jia, F. Meier, J. H. Dil, J. Osterwalder, B. Slomski, A. Bansil, H. Lin, R. J. Cava, and M. Z. Hasan, Topological phase transition and texture inversion in a tunable topological insulator, *Science* **332**, 560 (2011).
- [13] S. Y. Xu, C. Liu, N. Alidoust, M. Neupane, D. Qian, I. Belopolski, J. D. Denlinger, Y. J. Wang, H. Lin, L. A. Wray, G. Landolt, B. Slomski, J. H. Dil, A. Marcinkova, E. Morosan, Q. Gibson, R. Sankar, F. C. Chou, R. J. Cava, A. Bansil, and M. Z. Hasan, Observation of a

- topological crystalline insulator phase and topological phase transition in  $\text{Pb}_{1-x}\text{Sn}_x\text{Te}$ , [Nat. Commun. \*\*3\*\*, 1192 \(2012\)](#).
- [14] B. M. Wojek, M. H. Berntsen, V. Jonsson, A. Szczerbakow, P. Dziawa, B. J. Kowalski, T. Story, and O. Tjernberg, Direct observation and temperature control of the surface Dirac gap in a topological crystalline insulator, [Nat. Commun. \*\*6\*\*, 8463 \(2015\)](#).
- [15] J. L. Collins, A. Tadich, W. Wu, L. C. Gomes, J. N. Rodrigues, C. Liu, J. Hellerstedt, H. Ryu, S. Tang, S. K. Mo, S. Adam, S. A. Yang, M. S. Fuhrer, and M. T. Edmonds, Electric-field-tuned topological phase transition in ultrathin  $\text{Na}_3\text{Bi}$ , [Nature \*\*564\*\*, 390 \(2018\)](#).
- [16] S. Klemenz, S. Lei, and L. M. Schoop, Topological Semimetals in Square-Net Materials, [Annu. Rev. Mater. Res. \*\*49\*\*, 185 \(2019\)](#).
- [17] E. DiMasi, B. Foran, M. C. Aronson, and S. Lee, Stability of charge-density waves under continuous variation of band filling in  $\text{LaTe}_{2-x}\text{Sb}_x$  ( $0 \leq x \leq 1$ ), [Phys. Rev. B \*\*54\*\*, 13587 \(1996\)](#).
- [18] R. Singha, T. H. Salters, S. M. L. Teicher, S. Lei, J. F. Khoury, N. P. Ong, and L. M. Schoop, Evolving Devil's Staircase Magnetization from Tunable Charge Density Waves in Nonsymmorphic Dirac Semimetals, [Adv. Mater. , 2103476 \(2021\)](#).
- [19] S. Lei, V. Duppel, J. M. Lippmann, J. Nuss, B. V. Lotsch, and L. M. Schoop, Charge Density Waves and Magnetism in Topological Semimetal Candidates  $\text{GdSb}_x\text{Te}_{2-x-\delta}$ , [Adv. Quantum Technol. \*\*2\*\*, 1900045 \(2019\)](#).
- [20] K. Pandey, R. Basnet, J. Wang, B. Da, and J. Hu, Evolution of electronic and magnetic properties in the topological semimetal  $\text{SmSb}_x\text{Te}_{2-x}$ , [Phys. Rev. B \*\*105\*\*, 155139 \(2022\)](#).
- [21] Y. T. Qian, Z. Y. Tan, T. Zhang, J. C. Gao, Z. J. Wang, Z. Fang, C. Fang, and H. M. Weng, Layer construction of topological crystalline insulator  $\text{LaSbTe}$ , [Sci. China-Phys. Mech. Astron. \*\*63\*\*, 1 \(2020\)](#).
- [22] Y. Wang, Y. Qian, M. Yang, H. Chen, C. Li, Z. Tan, Y. Cai, W. Zhao, S. Gao, Y. Feng, S. Kumar, E. F. Schwier, L. Zhao, H. Weng, Y. Shi, G. Wang, Y. Song, Y. Huang, K. Shimada, Z. Xu, X. J. Zhou, and G. Liu, Spectroscopic evidence for the realization of a genuine topological nodal-line semimetal in  $\text{LaSbTe}$ , [Phys. Rev. B \*\*103\*\*, 125131 \(2021\)](#).
- [23] V. Brouet, W. L. Yang, X. J. Zhou, Z. Hussain, N. Ru, K. Y. Shin, I. R. Fisher, and Z. X. Shen, Fermi surface reconstruction in the CDW state of  $\text{CeTe}_3$  observed by photoemission, [Phys. Rev. Lett. \*\*93\*\*, 126405 \(2004\)](#).

- [24] V. Brouet, W. L. Yang, X. J. Zhou, Z. Hussain, R. G. Moore, R. He, D. H. Lu, Z. X. Shen, J. Laverock, S. B. Dugdale, N. Ru, and I. R. Fisher, Angle-resolved photoemission study of the evolution of band structure and charge density wave properties in  $\text{RTe}_3$  ( $\text{R}=\text{Y}, \text{La}, \text{Ce}, \text{Sm}, \text{Gd}, \text{Tb}, \text{and Dy}$ ), *Phys. Rev. B* **77**, 235104 (2008).
- [25] K. Y. Shin, V. Brouet, N. Ru, Z. X. Shen, and I. R. Fisher, Electronic structure and charge-density wave formation in  $\text{LaTe}_{1.95}$  and  $\text{CeTe}_{2.00}$ , *Phys. Rev. B* **72**, 085132 (2005).
- [26] C. D. Malliakas and M. G. Kanatzidis, Divergence in the Behavior of the Charge Density Wave in  $\text{RETe}_3$  ( $\text{RE} = \text{Rare-Earth Element}$ ) with Temperature and RE Element, *J. Am. Chem. Soc.* **128**, 12612 (2006).
- [27] J.-Q. Yan, B. C. Sales, M. A. Susner, and M. A. McGuire, Flux growth in a horizontal configuration: An analog to vapor transport growth, *Phys. Rev. Mater.* **1**, 023402 (2017).
- [28] P. Blaha, K. Schwarz, F. Tran, R. Laskowski, G. K. Madsen, and L. D. Marks, WIEN2k: An APW+lo program for calculating the properties of solids, *J. Chem. Phys.* **152**, 74101 (2020).
- [29] P. Blaha, K. Schwarz, G. Madsen, D. Kvasnicka, J. Luitz, R. Laskowski, F. Tran, and L. Marks, *WIEN2k, An Augmented Plane Wave + Local Orbitals Program for Calculating Crystal Properties* (2018).
- [30] J. P. Perdew, K. Burke, and M. Ernzerhof, Generalized Gradient Approximation Made Simple, *Phys. Rev. Lett.* **77**, 3865 (1996).
- [31] P. Giannozzi, S. Baroni, N. Bonini, M. Calandra, R. Car, C. Cavazzoni, D. Ceresoli, G. L. Chiarotti, M. Cococcioni, I. Dabo, A. D. Corso, S. D. Gironcoli, S. Fabris, G. Fratesi, R. Gebauer, U. Gerstmann, C. Gougoussis, A. Kokalj, M. Lazzeri, L. Martin-Samos, N. Marzari, F. Mauri, R. Mazzarello, S. Paolini, A. Pasquarello, L. Paulatto, C. Sbraccia, S. Scandolo, G. Sclauzero, A. P. Seitsonen, A. Smogunov, P. Umari, and R. M. Wentzcovitch, QUANTUM ESPRESSO: a modular and open-source software project for quantum simulations of materials, *J. Phys.: Condens. Matter* **21**, 395502 (2009).
- [32] P. Giannozzi, O. Andreussi, T. Brumme, O. Bunau, M. B. Nardelli, M. Calandra, R. Car, C. Cavazzoni, D. Ceresoli, M. Cococcioni, N. Colonna, I. Carnimeo, A. D. Corso, S. D. Gironcoli, P. Delugas, R. A. Distasio, A. Ferretti, A. Floris, G. Fratesi, G. Fugallo, R. Gebauer, U. Gerstmann, F. Giustino, T. Gorni, J. Jia, M. Kawamura, H. Y. Ko, A. Kokalj, E. Küçükbenli, M. Lazzeri, M. Marsili, N. Marzari, F. Mauri, N. L. Nguyen, H. V. Nguyen, A. Otero-De-La-Roza, L. Paulatto, S. Poncé, D. Rocca, R. Sabatini, B. Santra, M. Schlipf,

A. P. Seitsonen, A. Smogunov, I. Timrov, T. Thonhauser, P. Umari, N. Vast, X. Wu, and S. Baroni, Advanced capabilities for materials modelling with Quantum ESPRESSO, [J. Phys.: Condens. Matter](#) **29**, 465901 (2017).

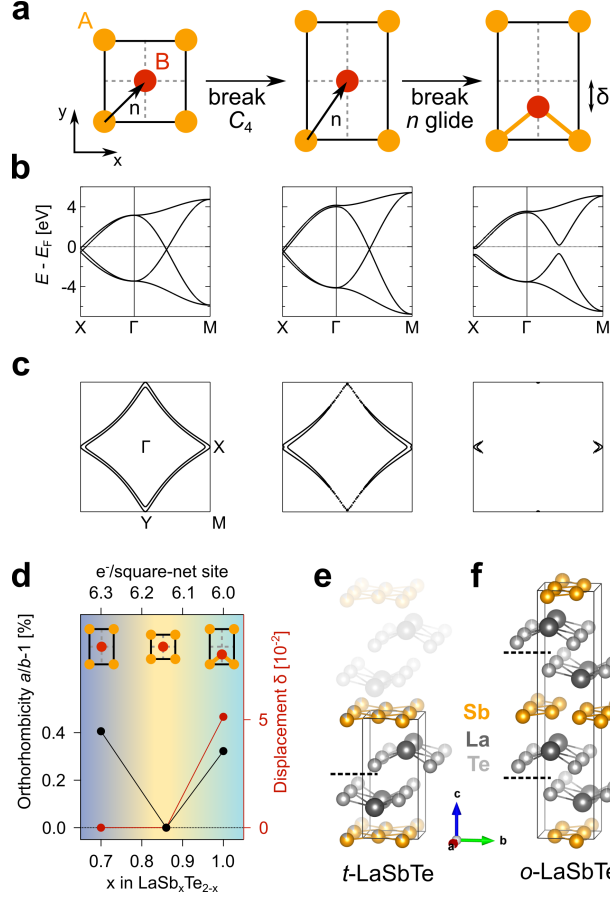


FIG. 1. **Gap opening of the square-net-derived nodal loop by symmetry lowering.**

**a** Minimal model for a square-net with two sublattices A and B that is undergoing symmetry lowering from an ideal square-net to zig-zag chains by consecutive breaking of  $C_4$  and  $n$  glide symmetry. **b** Breaking of  $C_4$  symmetry causes minor changes to the band structure along X- $\Gamma$ -M and leaves the nodal loop gapless. Only breaking of  $n$  glide symmetry causes the opening of a large gap in the nodal loop. **c** Similarly, the diamond shaped Fermi surface of the ideal square-net experiences only minor warping by removal of  $C_4$  symmetry, whereas subsequent breaking of  $n$  glide symmetry causes a major reduction in Fermi surface volume by gapping out large parts of the Fermi surface. **d** All three stages of the model are experimentally realized in  $\text{LaSb}_x\text{Te}_{2-x}$  as a function of antimony concentration  $x$ . The values for orthorhombicity and displacement, as determined from single crystal XRD, indicate breaking of  $C_4$  and  $n$  glide symmetry, respectively. The partial substitution of antimony with tellurium for  $x < 1$  effectively increases the electron filling of the square-net layer. **e,f** Crystal structures of  $t$ -LaSbTe and  $o$ -LaSbTe, corresponding to  $x=0.9$  and 1, where the breaking of antimony square-nets into zig zag chains switches the topology, driving the transition from gapless to gapped nodal loop. These antimony layers lie below the surface after cleavage along the dashed lines. 16

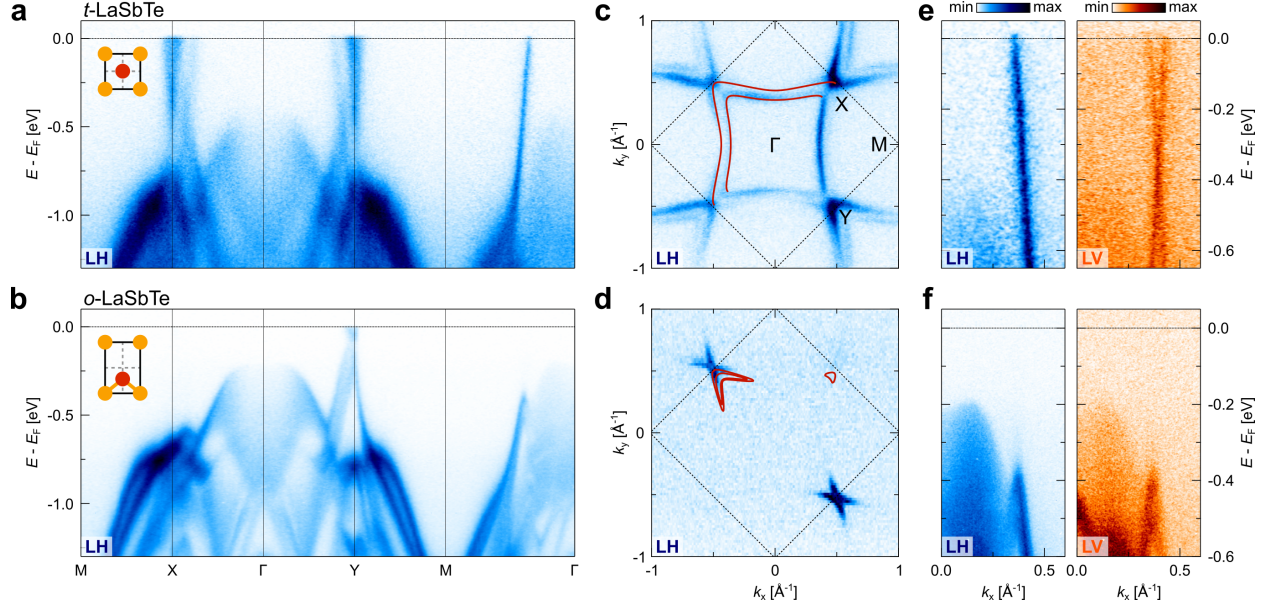
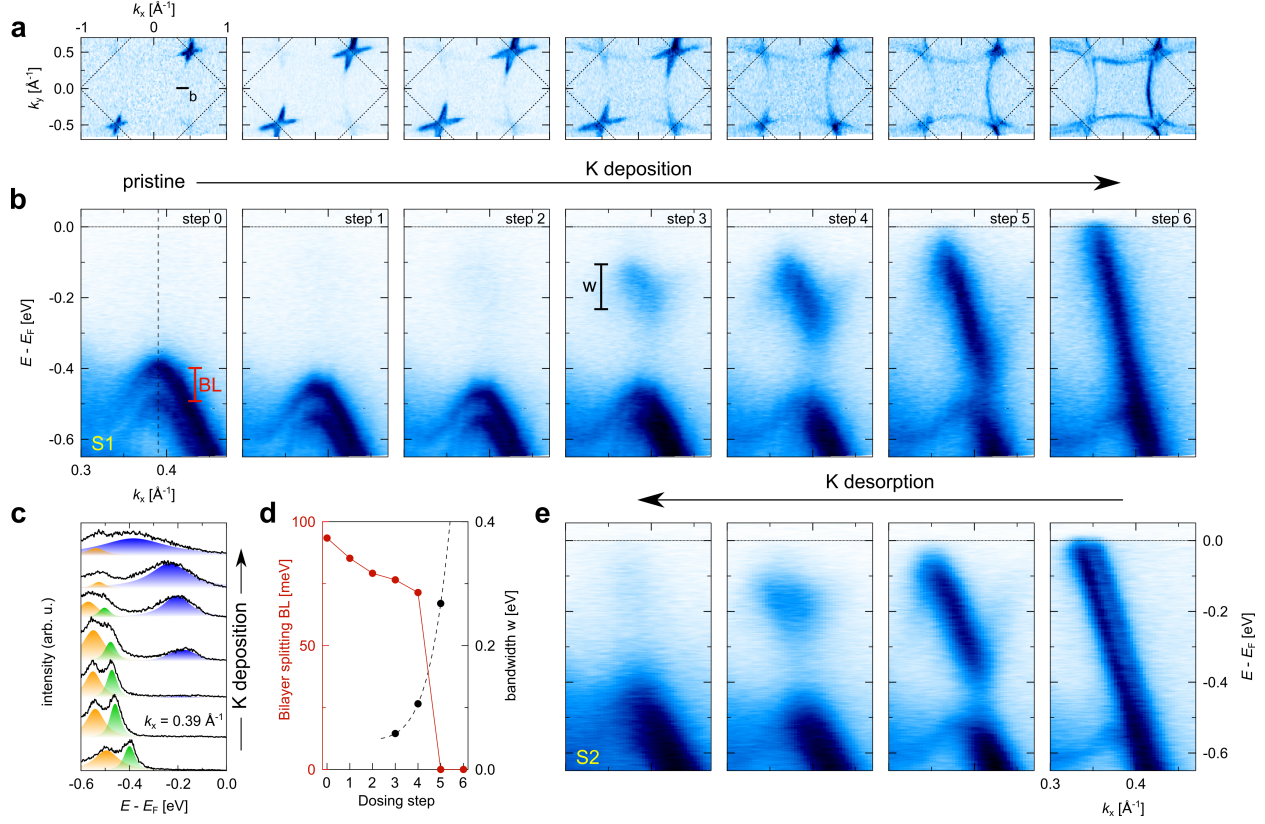


FIG. 2. **Topological phase transition from gapless to gapped nodal loop in  $\text{LaSb}_x\text{Te}_{2-x}$ .** **a, b** ARPES spectra of  $t$ -LaSbTe and  $o$ -LaSbTe, respectively, along a high symmetry path. Bands forming the nodal loop are gapless and cross the Fermi level along  $\Gamma$ -M and  $\Gamma$ -X/Y in  $t$ -LaSbTe. Breaking of  $n$  glide symmetry in  $o$ -LaSbTe causes these bands to open a massive gap at the X point and along  $\Gamma$ -M. **c, d** Fermi surfaces of  $t$ -LaSbTe and  $o$ -LaSbTe; the two concentric diamond shaped sheets in  $t$ -LaSbTe gap out almost entirely upon breaking of  $n$  glide symmetry in  $o$ -LaSbTe, in excellent agreement with DFT calculations (red lines overlaid). The black dashed line indicates the Brillouin zone. **e** Zoom-in spectra along  $\Gamma$ -M for  $t$ -LaSbTe acquired with linear horizontal (LH) and linear vertical (LV) polarization to probe matrix element effects (note that all data in panels **a-d** were measured with LH polarization). Both branches of the gapless nodal loop are visible. **f** Same as panel **e** but for  $o$ -LaSbTe; with both LH and LV polarization we observed a  $>400$  meV gap in the nodal loop along  $\Gamma$ -M.



**FIG. 3. Topological switching by *in situ* control of crystalline symmetry.** **a** Evolution of the Fermi surface of *o*-LaSbTe with stepwise potassium deposition. All data presented in this figure were acquired with LH polarization. After an initial increase in Fermi surface volume caused by the electron doping, the spectral weight redistributes until two concentric diamond shaped sheets with fourfold symmetry are formed in step 6. **b** Evolution of the spectra along  $\Gamma$ -M (black line in **a**). The nodal loop gap closes via the formation of in-gap states that fill up the entire gap in step 6. Together with the fourfold symmetric Fermi surface, this indicates restoration of *n* glide symmetry in the top antimony layer. **c** Representative energy distribution curves at  $k_x = 0.39 \text{ \AA}^{-1}$  (black dashed line in **b**) for each dosing step and fits to pseudo-Voigt line shape. The upper band of the initial bilayer-split valence bands merges with the in-gap states to form the gapless nodal loop. **d** Reduction and disappearance of bilayer splitting with increasing potassium deposition, as extracted from panel **c**. At the same time, the bandwidth of the in-gap states increases to the full width of the initial gap in *o*-LaSbTe. The black dashed line is a guide to the eye. **e** Desorption of potassium transforms the gapless nodal loop back to the initial gapped state, indicating a fully reversible switching of topology, with the transition between gapless and gapped nodal loop mediated by manipulation of *n* glide symmetry. Data in panels **a-d** were measured on sample S1, and in panel **e** on sample S2.

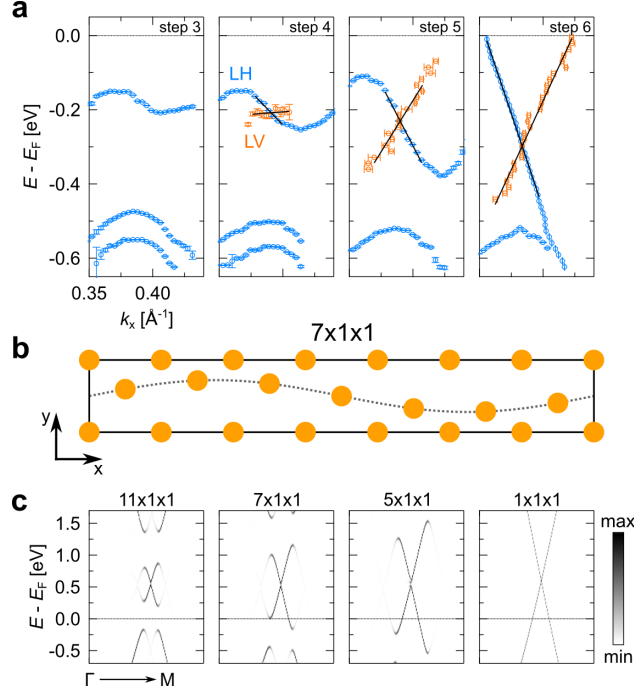


FIG. 4. **Continuous tuning of  $n$  glide symmetry.** **a** Band dispersions obtained from fits of spectra along  $\Gamma$ -M acquired with LH (blue symbols, same spectra as in Fig. 3b) and LV polarization (orange symbols, spectra in SM), for potassium dosing steps 3-6. Black lines are linear fits around the band crossings of the in-gap states. Steps 4 and 5 exhibit the coexistence of Dirac cone and nodal loop gap, which cannot be explained by the model in Fig. 1. The observation of back folded bands in the in-gap states in steps 3-5 indicates CDW phases. **b** Structure of the proposed CDW model that qualitatively describes the data in panel **a**. Shown here is a  $7 \times 1 \times 1$  supercell of monolayer antimony with sinusoidal variation of the center Sb's  $y$  coordinate. The amplitude of the variation is exaggerated by factor of 4 for visualization. **c** Band structures of the CDW supercells with varying size of supercell, after unfolding and projection onto  $p_{x,y}$  states. In-gap states show band folding similar to the experimental data in panel **a**. With decreasing size of the CDW supercell the bandwidth of the in-gap states increases, replicating the trend in the experimental data. Note that the  $1 \times 1 \times 1$  "supercell" corresponds to pristine  $t$ -LaSbTe. Fermi level shifts observed in the data in panel **a** are ignored in the model.